QUERY FORM

JOURNAL: Journal of Neural Engineering

AUTHOR: C C Javier *et al*

TITLE: Characterization of vagus nerve active fibers during seizure in rats

ARTICLE ID: ae30aa

Your article has been processed in line with the journal style. Your changes will be reviewed by the Production Editor, and any amendments that do not comply with journal style or grammatical correctness will not be applied and will not appear in the published article.

The layout of this article has not yet been finalized. Therefore this proof may contain columns that are not fully balanced/matched or overlapping text in inline equations; these issues will be resolved once the final corrections have been incorporated.

Q1: Please check that the names, ORCID iDs, and contribution data for all authors are correct, and that all authors are linked to the correct affiliations. Please also confirm that the correct corresponding author has been indicated. This is your last opportunity to review this information before your article is published.

Q2: Please provide the City in affiliation [3].

Q3: Please note: we do not edit supplementary data, the files will be hosted in the format you supplied. If you would like to supply new files please send them with your proof corrections.

Q4: Following journal style, the supplementary data file Supplementary_materials CLEAN.docx will be renamed to jneae30aasupp1.docx and presented as:
Supplementary data. (8.5 MB DOCX)
If required, please provide replacement text for "Supplementary data" (maximum 30 characters). You may also provide a short description of the file if further information is necessary (maximum 30 words). This will appear after the details above.

Q5: This journal requires that the following subheadings be added to the abstract: Objective, Approach, Main results and Significance. Please indicate where, within your abstract, these headings should be inserted, or how existing subheadings can be modified.

Q6: References were not cited sequentially. Hence, references have been renumbered from Reference 46. Please check.

Q7: If an explicit acknowledgment of funding is required, please ensure that it is indicated in your article. If you already have an Acknowledgments section, please check that the information there is complete and correct.

Q8: The information in the Funding Metadata section is a list of funder names and grant numbers that will be registered on your behalf when the article is published. This information will not be shown in the article text. If an explicit acknowledgment of funding is required, please ensure that it is provided in an Acknowledgments section in your article. Please check that the funding information below is correct for inclusion in the article metadata.
Walloon Region (Belgium)

Q9: Please note that Crossref and PubMed databases have been used to validate the references and mismatches have been updated in the following references: [6,10,14–16,19,23,40,43–45,48,54,57,59,62,65,68]. Please check and confirm that these have been done correctly.

Q10: Only minor, essential corrections to your article can be made at this stage. Minor changes are those that do not significantly affect either the scientific meaning of the article or its bibliographic identity. No changes can be made to authorship (other than those covered by our Name Change Policy) and references cannot be added or removed unless in response to a specific proof query. We reserve the right to deny correction requests from authors which we deem in breach of our ethical policy.

Q11: Please provide the volume number in reference [53].

IOP Publishing J. Neural Eng. 0 (2025) xxxxxx https://doi.org/10.1088/1741-2552/ae30aa

Journal of Neural Engineering

PAPER

RECEIVED
18 December 2024

REVISED
5 November 2025

ACCEPTED FOR PUBLICATION
23 December 2025

PUBLISHED
xx xx xxxx

Characterization of vagus nerve active fibers during seizure in rats

Javier Chávez Cerda[1,*], Elena Acedo Reina[2], Cedric Luppens[1], Louis Vande Perre[1], Romain Raffoul[1], Maxime Verstraeten[1], Enrique Germany Morrison[2], Hugo Smets[1], Pascal Doguet[1], Jérôme Garnier[3], Jean Delbeke[2], Riëm El Tahry[2] and Antoine Nonclercq[1]

[1] Bio-, Electro-and Mechanical-Systems (BEAMS), Université Libre de Brussels, Brussels, Belgium
[2] Institute of Neurosciences (IoNS), Université Catholique de Louvain, Brussels, Belgium
[3] Synergia Medical SA, Mont -Saint-Guibert, Belgium
[*] Author to whom any correspondence should be addressed.

E-mail: javier.chavez.cerda@ulb.be

Keywords: vagus nerve electroneurogram, fiber size, compound action potential, fiber activity occurrence, seizure detection, close-loop stimulation

Supplementary material for this article is available online

Abstract

Epilepsy affects approximately 70 million individuals worldwide. Vagus nerve activity is known to be modulated by seizures; however, the types of fibers that are activated during seizures remain unknown. This work compares the electrical activity of the vagus nerve before, during, and after seizures in epileptic rats. Six rats experiencing pentylenetetrazol-induced epilepsy seizures and two rats under saline solution were investigated. Action potentials (AP) identified by template matching were sorted according to the fiber type they are deemed to originate from. AP templates were based on a 3D COMSOL simplified model of the vagus nerve. Model templates were established for fibers of different diameters based on histology. Correspondences are thus established based on specific fiber diameters. During seizures, an increase in the percentage of occurrence of APs was observed for 2 μm and 3 μm fibers, while a decrease was observed for 4 μm, 5–6 μm, and 7–11 μm fibers. This was not observed in the rat group under saline solution. The increase in smaller diameter sizes is believed to be linked to an increase in autonomic activity. These findings contribute to a better understanding of vagus nerve dynamics during epileptic seizures and highlight the potential of vagus nerve activity as a physiological marker for seizure detection and monitoring. This would be of particular interest in vagus nerve stimulation to control any closed-loop form of therapy. This work provides a foundation for developing novel diagnostic and therapeutic approaches in epilepsy management.

1. Introduction

Affecting around 70 million people, epilepsy is one of the most common neurological disorders in the world [1]. This condition is defined as a brain disease characterized by an enduring predisposition to generate recurrent and unprovoked seizures [2]. Seizures are clinical manifestations such as abnormal or automatic movements, strange sensations and feelings, unusual behavior, and/or loss of consciousness associated with abnormal electroencephalogram (EEG) signals [3]. People with epilepsy are thus strongly affected in their daily lives, suffering an increased mortality rate [2] as well as social stigma and discrimination [4].

The most common treatment to address epilepsy is the use of antiepileptic drugs (AEDs), but these remain ineffective for 30% of patients [5–8]. In addition, side effects and toxic complications of the AEDs often limit their use [9–11]. Several surgical procedures can be proposed for these patients in an attempt to remove or disconnect brain tissue that initiates or propagates seizures. However, this is not feasible in about 50% of the cases [12]. In addition, despite some remarkable successes, there are patients who experience only modest or no improvement after surgery [13–15]. Neuromodulation is an alternative therapy to antiseizure drugs and surgery, achieving a 50% or greater seizure reduction in 35%–45% of patients

within the first year and in 60%–75% of patients over longer periods [16]. In recent decades, vagus nerve stimulation (VNS) has been shown to reduce seizure severity and frequency in a significant proportion of cases. The vagus nerve is broadly connected to various brain regions and has shown a potential for modulation of seizure activity [17]. Stimulating the vagus nerve may help decrease the hyperexcitability of neurons in the brain, increasing the production of GABA and norepinephrine neurotransmitters, which have an inhibitory effect [18, 19]. Clinical trials demonstrate that 20%–40% of patients achieve a greater than 50% reduction in seizure frequency in the first year of use. These results improve during chronic VNS treatment, while the number of concomitant AEDs necessary to maintain satisfactory seizure control decreases [20].

Most commercial VNS devices on the market currently operate with an open-loop approach, which means that a fixed level of VNS is delivered intermittently [17, 21] at specified, pre-programmed intervals. There is no adaptive adjustment based on the physiological response of the patient [22]. The acute abortive effect (that is stopping or reducing the severity of an already ongoing seizure) of VNS has been previously demonstrated in humans [23, 24] and animal studies [25], strengthening the expectation that an automated seizure detection controlling on-demand VNS would clearly be beneficial. In addition, VNS side effects happened during electrical pulse delivery, such as hoarseness, coughing, and laryngeal paraesthesia [21]. Closed-loop VNS, i.e., stimulating only at the occurrence of a seizure, could be associated with greater seizure reduction and fewer side effects and have more favorable clinical outcomes than open-loop stimulation [22, 26]. Currently, closed-loop stimulation, as applied in AspireSR™ Model 106 and the SenTiva™ Model 1000, is based on heart rhythm changes [27]. While the use of increased heart rate as a biomarker for seizure detection shows promise, challenges remain in differentiating ictal tachycardia from a physiological rise in heart rate [27]. Only half of the seizures induced significant tachycardia [28] (>20% increase in the heart rate) and moreover, there is considerable variability in ictal heart rate changes amongst and within patients [29].

The vagus nerve electrical activity or vagus nerve electroneurogram (VENG) emerges as a promising candidate for monitoring the bidirectional neural signal traffic between the brain and peripheral organs. Several studies suggest the possibility of extracting different physiological signals from the vagus nerve, with examples for blood pressure and respiration cycles [30–32]. The vagus nerve is also the primary parasympathetic output of the nervous system, while seizures are often associated with autonomic manifestations. Previous studies in rats suggest that VENG changes during seizures [33–35], and in humans, elevated cardiac parasympathetic activity has been recorded during sub-clinical seizures [36], and a surge in parasympathetic activity has been observed just before fatal seizures [37]. Thus, seizure-related signals can be expected to be found in the vagus nerve. There is also a practical incentive to record from the nerve implanted for the VNS therapy. Therefore, many reasons exist to explore the possibilities for early seizure detection offered by the vagus nerve.

The histology and physiology of the vagus nerve are reasonably well documented in humans, with different fiber sizes, conduction velocities, activation thresholds, and the motor, sensory, or autonomic functions associated with specific fiber types [38, 39]. The myelinated fiber population at the cervical vagus nerve level is typically divided into different categories based on size, namely small-diameter (<3 μm), medium-diameter (3–9 μm), and large-diameter (>10 μm) fibers for humans [40], relating the small myelinated fiber diameter to autonomic type and the medium and larger diameter to motor and sensory type [39]. Since seizures are associated with autonomic manifestations, they probably involve changes in the smallest myelinated fibers. Given the similar fiber diameter distribution in vagus nerve structure between humans and rats, the animal model used in this study, findings may be translatable and provide meaningful insights applicable to humans.

Template similarity has been applied previously to analyze the VENG [30, 41, 42]. Our group has proposed to analyze the VENG recorded in healthy anesthetized rats based on templates extracted from VENG simulations in COMSOL. Different fiber diameters have been modeled [42]. The present work applies the same method to characterize the changes in firing patterns as a function of the fiber's diameter before, during, and after a seizure in rats. Besides understanding vagus nerve dynamics during epilepsy seizures, finding a potentially robust physiological marker for seizure detection is also a major goal.

2. Methods

2.1. Acute recording data

The data were collected from eight male Wistar rats (weight of 424.4 $\pm$ 31.7 gr, age of 3.9 $\pm$ 0.9 months) [30], the University Health Sciences Sector Laboratory Animal Protection Committee approved the experimental procedures under the reference 2018/UCL/MD/001. The animals were housed under a 12 h day/night cycle with controlled temperature and humidity and 'ad libitum' access to food and water.

For the surgery, all animals were anesthetized using a combination of ketamine (60 mg kg^{-1})

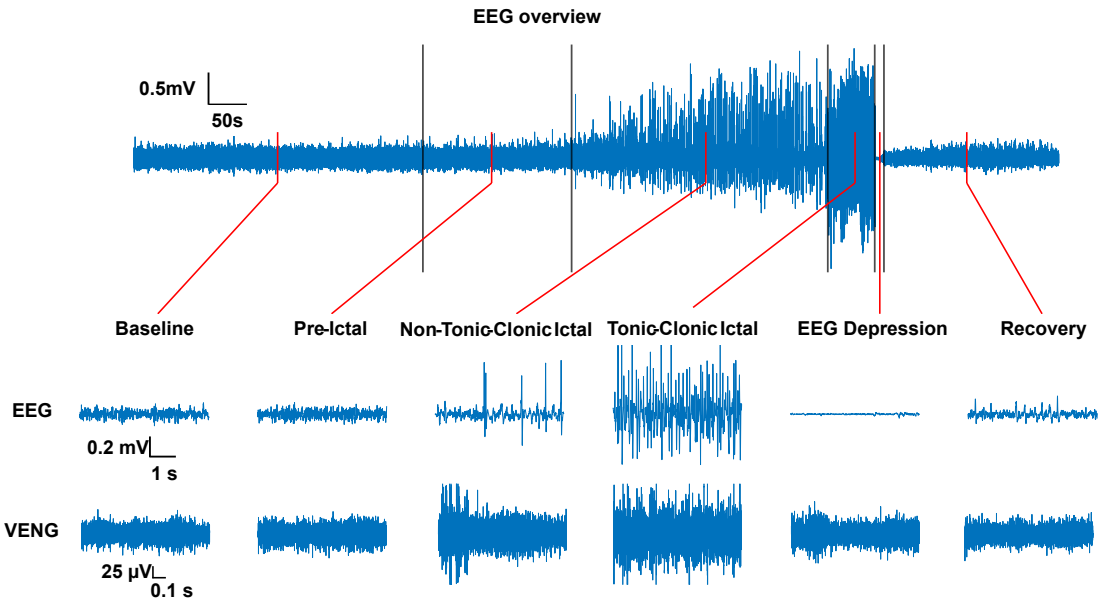

Figure 1. Electroencephalogram (EEG) and vagus nerve electroneurogram (VENG) evolution in time using the PTZ model. The six stages can be identified by visual inspection on the EEG.

and xylazine (7 mg kg^{-1}) administered intraperitoneally (i.p.). The animals were implanted with homemade epidural EEG electrodes, consisting of a 4.8 mm stainless-steel screw (Bilaney, Germany) that were implanted at specific coordinates relative to the Bregma: for the frontal electrode (+) [anteroposterior (AP) +2 mm, mesolateral (ML) +3 mm], reference electrode (Ref) [AP +6 mm, ML 0 mm], and ground electrode (GND) [AP −5 mm, ML +3 mm] in the parietal region. EEG was recorded differentially between left frontal and parietal electrode. For VENG recordings, a tripolar micro-cuff electrode (Microprobes, Gaithersburg, USA) was implanted on the left cervical vagus nerve, with an inter-electrode distance of 2 mm. The central contact (B) served as the reference (negative), while the two outer contacts, caudal (A) and rostral (C), were used as the recording (positive) electrodes. This configuration yielded two differential signals (A–B and C–B) and subtracted, deriving a 4 mm bipolar recording between the caudal and rostral contacts ((A–B)—(C–B) = A–C). A set of custom-made amplifiers were used. This set consisted out of two VENG and one EEG amplifiers. The amplifiers had a bandwidth of 12–12 000 Hz for VENG, and 12–170 Hz) for EEG, having a nominal gain of 800 V/V.

During the surgery, depth of anesthesia was controlled by the withdrawal reflex upon noxious paw stimulation and maintained by a booster injection of ketamine (60 mg kg^{-1}) i.p. Five minutes later, intravenous (i.v.) saline solution was infused to all rats (0.5 ml min^{-1} kg^{-1}) for 10 min, used as the baseline interval for all rats.

Then, in six out of eight rats (seizure group), the i.v. saline solution infusion was switched to 10 mg ml $^{-1}$ i.v. of pentylenetetrazol (PTZ) at the same infusion rate, to induce acute seizures [30, 34]. PTZ infusion was maintained until the animal reached the tonic–clonic phase of the seizure, and recordings were continued for 10 min after the EEG had recovered from the postictal depression. For two of the eight rats (control group), the saline solution infusion was continued for an additional 10 min, trying to mimic the PTZ infusion time (9.01 ± 1.62 min). Then, the recording was extended by 10 min for recovery ensuring a similar duration for both the PTZ and the control groups. The VENG signals were recorded at a sampling frequency of 80 kHz, and the EEG was sampled at 250 Hz. To counter the noise artifact, the VENG signal was filtered using a 2nd order Butterworth 300 Hz–3 kHz bandpass filter, with zero-phase shift.

The recordings were divided into several stages based on the EEG and a simultaneous video recording [30]. For the seizure

group, the six stages defined, as illustrated in figure 1, include:

- **Baseline interval:** This interval occurs between the start of i.v. saline and the switch to i.v. PTZ. In the EEG, occasional low-amplitude spikes are characteristic of this interval (10 min).
- **Preictal interval:** The preictal interval gradually develops after the start of i.v. PTZ. A slight increase in the number of low-amplitude spikes characterizes this interval.
- **Non-tonic–clonic ictal interval:** The determination of this interval is based on a sustained increase in spike frequency over 0.25 Hz for a duration exceeding 10 s. Moreover, there is a subsequent rise

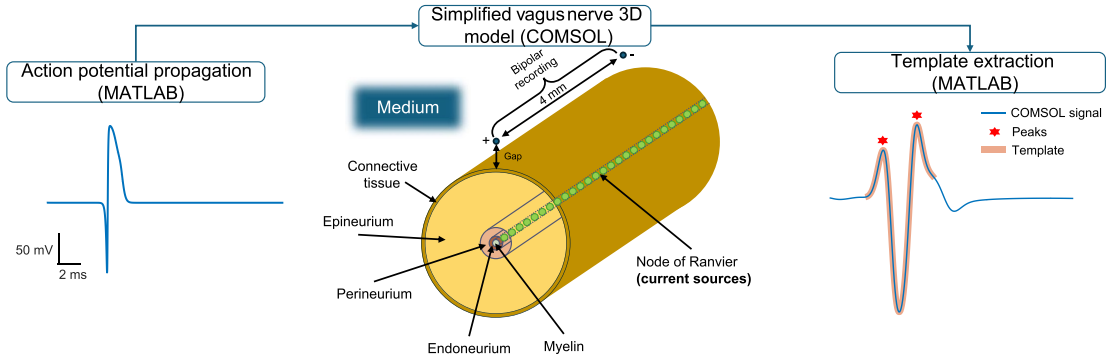

Figure 2. Template extraction from Matlab and COMSOL simulations (not to scale).

in spike frequency and amplitude, accompanied by muscle twitches. The onset of this interval is also considered the onset of the seizure.

- **Tonic–clonic ictal interval:** The tonic–clonic ictal interval is characterized by the abrupt onset of continuous repetitive (5–10 Hz) high amplitude EEG spikes. These spikes have an average amplitude 10 times greater than the standard deviation of the baseline activity. Clonic muscle activity is observed during this interval. The cessation of the last burst of continuous high-amplitude spikes determines the end of the tonic–clonic phase.
- **EEG depression:** This interval is characterized by a global reduction in EEG activity immediately after the end of the tonic–clonic phase.
- **Recovery:** The recovery interval is characterized by a gradual recovery of EEG activity. It is determined by the first occurrence of spikes exceeding a threshold of one time the standard deviation of baseline activity (10 min).

For the control group, three distinct stages are defined:

- **Baseline interval:** The first stage corresponds to the baseline, which mirrors the baseline in the rats under PTZ (10 min).
- **Saline interval:** The second stage involves the administration of saline, in contrast to the PTZ received by the other rats (10 min).
- **Recovery:** Lastly, the third stage encompasses the 'recovery' period following the cessation of i.v. saline injection (10 min).

The objective is to analyze the activity of the vagus nerve during each stage, for the control and PTZ groups, and compare the findings across all stages. We analyzed offline for respiratory-related bursting activity in the VENG during baseline and recovery intervals to verify adequate contact between the electrode cuff and the vagus nerve. The consistent appearance of these respiration bursts, which are features of vagus nerve recordings in the literature [31, 32, 34, 43], served as a qualitative indicator of stable electrode-nerve contact. Additionally, this methodology previously confirmed the authenticity of the VENG signal by comparing it with the EMG signal recorded around the nerve, revealing a consistent phase lag between the two [34].

2.2. Action potential (AP) profile from nerve model simulation

The AP profiles, used as templates in this work, were extracted from nerve model simulations based on our previous work [42]. First, the AP propagation equations were computed for myelinated fibers only. Then, a 3D model of the vagus nerve, which included dynamic AP propagation in a centered, myelinated fiber, was developed based on the geometry of the vagus nerve. Finally, the AP profile was extracted from the model. The diagram of this process is shown in figure 2.

2.2.1. AP propagation

An AP propagation was modeled in Matlab 2024 for different fiber diameters using the Wesselink–Schwarz model [44], adapted to mammal fibers by Wesselink [45] (see the appendix A for the equations), as shown in figure 2 (left).

Modeling was conducted for fiber diameters ranging from 2 μm to 11 μm, in steps of 1 μm, in agreement with histological ranges. This range aligns with the work of Smets *et al* [42], who reported that 90% of detected APs fell within this range, and with the findings on myelinated fiber diameters in the cervical vagus nerve of Wistar-Kyoto rats [47]. To account for the structural properties of the axon, the internode length ($L_{\text{internode}}$), was assumed to be 100 times the diameter of the fiber [48], the axon diameter (d_{axon}) was assumed to be 0.6 times the diameter of the fiber [49], and the node of Ranvier length (l_x) was set to 1.5 μm [50]. The model parameters were set to a physiological temperature (T) of 305.05 K (31.9 °C),

Table 1. Electrical conductivities of nerve layers and their dimensions (D_O: outer diameter, D: diameter, L: length, t: thickness, fd: fiber diameter in μm). Adapted from [46], Copyright (2016), with permission from Elsevier.

Tissue type	Conductivity [S m−1]	Dimensions (μm)
Medium	2	D_O: 10 000 t: 4760
Connective tissue	0.16	D_O: 480 t: 40
Epineurium	0.054	D_O: 400 t: 155
Perineurium	5.668×10^{-3}	D_O: 90 t: 25
Endoneurium	0.08 (radial) 0.5 (longitudinal)	D_O: 40 t: 10
Myelin	2.25×10^{-7}	L: 100*fd D: 20
Cytoplasm	0.53	L: 5*fd D: 20

measured around the vagus nerve, using a thermocouple type T (Data acquisition 34 970 A, Keysight Technologies) with an accuracy of 0.1 °C. The number of nodes of Ranvier modeled per fiber diameter was 398, ensuring complete 1D AP propagation along the fiber.

The model was implemented in Matlab 2024 (Mathworks), using the function 'ode23' to solve the system of ordinary differential equations via the Runge–Kutta (2,3) method, with a step time of 5μsec. Once the model was solved, the computed current values at each node of Ranvier () were obtained. The current density per node was computed (by dividing $I_{NR,x}$ with the inter-nodal volume).

2.2.2. 3D vagus nerve model

A vagus nerve geometry was reproduced in a FEM using COMSOL Multiphysics 6.2, as shown in figure 2 (middle). See Appendix B for equations. The nerve had a diameter of 400 μm [51], and was sufficiently long (0.206 m) to prevent boundary issues during AP propagation [52]. The parameters of the nerve's constituent layers were taken from [46] and the geometries were based on [42] (see table 1).

The model includes an epineurial layer to provide a standardized anatomical framework commonly found in many mammalian species, thereby enhancing the generalizability and translational potential of the simulations. However, the epineural layer has a negligible impact on the AP waveform (see figure S3), suggesting that it may also be applicable in rats. For simplicity, simulations considered only one fiber diameter at a time. The simulated fiber was positioned at the center of the nerve model.

Each node of Ranvier served as an input for current density (A m^3), with the current density values dynamically set based on the results of the Matlab model. COMSOL sends a request to MATLAB to retrieve the current density at specified spatial coordinates and time points. MATLAB then performs time and spatial interpolation using precomputed current density data to estimate the values at the requested locations and times.

Using the module Electrical Current module of COMSOL, the potential distribution based on the implemented vagus nerve geometry was computed, with a time step of 10 μs. The voltage reference ($V = 0$) was set on the surface of the model (medium), having distributed impedances (see appendix B.5). The mesh used in all simulations was a tetrahedral mesh with a minimum element size of 20 μm, chosen as a compromise between accurately representing the geometry and maintaining feasible computational requirements for the large 3D model.

In our FEM simulations, the potential at any point of the nerve geometry represents the superimposed contribution of every Nodes of Ranvier, meaning that even single-point electrodes capture a spatially integrated signal. The potential between 2 single points (4 mm separation) was computed. The single points positions and the simulation times per fiber diameter are given in appendix C.

2.2.3. Template extraction

The COMSOL signal, defined as the voltage difference between two points corresponding to the electrode contact positions (4 mm apart) on the geometry surface, was obtained for each fiber diameter. The COMSOL signal was filtered using a 2nd-order Butterworth bandpass filter (300 Hz–3 kHz) with zero-phase shift. The two highest peaks in the filtered signal were then identified, defining the width of the template. The start of the template was set a fixed number of samples before the first peak, and the end was set a fixed number of samples after the second peak, to include the surrounding signal. The number of surrounding samples before the first peak and after the second peak was adjusted for each template to ensure all templates had the same total length of 139 samples, while keeping the width centered as possible. Each template was defined as the section of the COMSOL signal between the two indices, as seen in figure 2 (right).

Each template represented the expected AP for a given fiber diameter, allowing the identification of that specific fiber diameter activity in the VENG signal. However, some templates could detect the same AP, causing ambiguities in fiber identification. To address this, each template was cross-correlated with each COMSOL signal to assess similarity (measured as the peak in the normalized cross-correlation). A threshold of maximal acceptable similarity was set to 0.975. Table 2 shows the maximum normalized cross-correlation values.

Table 2. Maximum absolute cross-correlation matrix between the templates and the COMSOL signals. The bold numbers show an absolute cross-correlation over the threshold of similarity. The bordered cells show no overlap in high correlation values (>0.975) for the different templates.

		COMSOL signal									
		2 μm	3 μm	4 μm	5 μm	6 μm	7 μm	8 μm	9 μm	10 μm	11 μm
Templates	2 μm	**1.000**	0.649	0.633	0.606	0.590	0.578	0.575	0.579	0.561	0.584
	3 μm	0.746	**1.000**	0.878	0.737	0.651	0.599	0.561	0.570	0.530	0.577
	4 μm	0.737	0.878	**1.000**	0.965	0.923	0.889	0.859	0.852	0.831	0.843
	5 μm	0.709	0.737	0.965	**1.000**	**0.989**	0.974	0.958	0.952	0.939	0.942
	6 μm	0.671	0.651	0.923	**0.989**	**1.000**	**0.996**	**0.988**	**0.981**	0.974	**0.977**
	7 μm	0.649	0.599	0.889	0.974	**0.996**	**1.000**	**0.997**	**0.993**	**0.990**	**0.990**
	8 μm	0.655	0.561	0.859	0.958	**0.988**	**0.997**	**1.000**	**0.995**	**0.994**	**0.994**
	9 μm	0.634	0.570	0.852	0.952	**0.981**	**0.993**	**0.995**	**1.000**	**0.997**	**0.997**
	10 μm	0.627	0.530	0.831	0.939	0.974	**0.990**	**0.994**	**0.997**	**1.000**	**0.996**
	11 μm	0.615	0.576	0.843	0.942	**0.977**	**0.990**	**0.994**	**0.997**	**0.996**	**1.000**

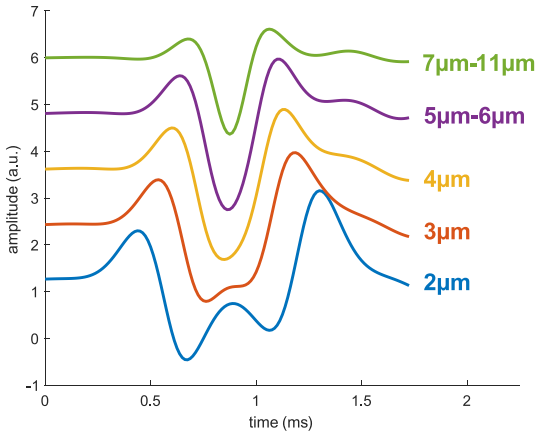

Figure 3. Templates selected for action potential detection.

The templates for 2 μm, 3 μm, and 4 μm fibers did not show high similarity with other COMSOL signals. However, templates for 5–11 μm fibers exhibited high similarity with multiple COMSOL signals, indicating they represented groups of fiber activations rather than single fibers. To avoid overlapping groups, the 5 μm template (representing 5 μm and 6 μm fibers) and the 10 μm template (representing 7–11 μm fibers) were selected. Ultimately, the chosen templates for AP detection were 2 μm, 3 μm, 4 μm, 5 μm (covering 5–6 μm), and 10 μm (covering 7–11 μm). Figure 3 shows the selected templates for AP detection.

2.3. AP detection algorithm

APs were detected on the VENG signal using a template-matching algorithm [41]. The VENG signal was cross-correlated with each template defined in the previous section separately. Then, the normalized cross-correlation maxima, with a minimum value of 0.7, were chosen as AP candidates. If one AP is detected with multiple templates, it is assigned to the template with the highest correlation value. The pseudocode and the overall methodology are illustrated in figure 4.

2.4. Statistical tools

Considering the small sample size in this study, a non-parametric test is recommended. The Kruskal–Wallis test was used for statistical comparisons across stages, as it is suitable for non-normally distributed data [53]. For post-hoc multiple comparisons, Dunnett's correction was applied [54], since the comparisons were performed only against the baseline state. The Wilcoxon rank-sum test was used to compare the control and PTZ group. A significance level of $\alpha = 0.05$ was used. Matlab 2024 provided these statistical tools.

3. Results

3.1. Occurrences of active fibers in the control group

Figure 5 shows the occurrence of active fibers in the control group for each stage. The percentage of occurrence showed no significant differences across stages for any fiber (2 μm, p-value $= 0.651 > 0.05$; 3 μm, p-value $= 1.0 > 0.05$; 4 μm, p-value $= 1.0$; 5–6 μm, p-value $= 1.0$; 7–11 μm, p-value $= 1.0$). Similarly, the post-hoc comparison with the baseline revealed no significant changes for any fiber (see table 3 for details). Similarly, for the absolute occurrence (number of AP detected/sec), there were no significant changes across the stages either (see figure S-1 in the supplementary materials).

3.2. Occurrences of active fibers in the seizure group

The percentage of APs detected per fiber diameter showed significant differences across the different stages, with respect to baseline, as shown in figure 6. There is a discernible change in the occurrence of detection between baseline and seizures, particularly during the tonic–clonic phase. This phase exhibits an alteration across all active fiber diameters.

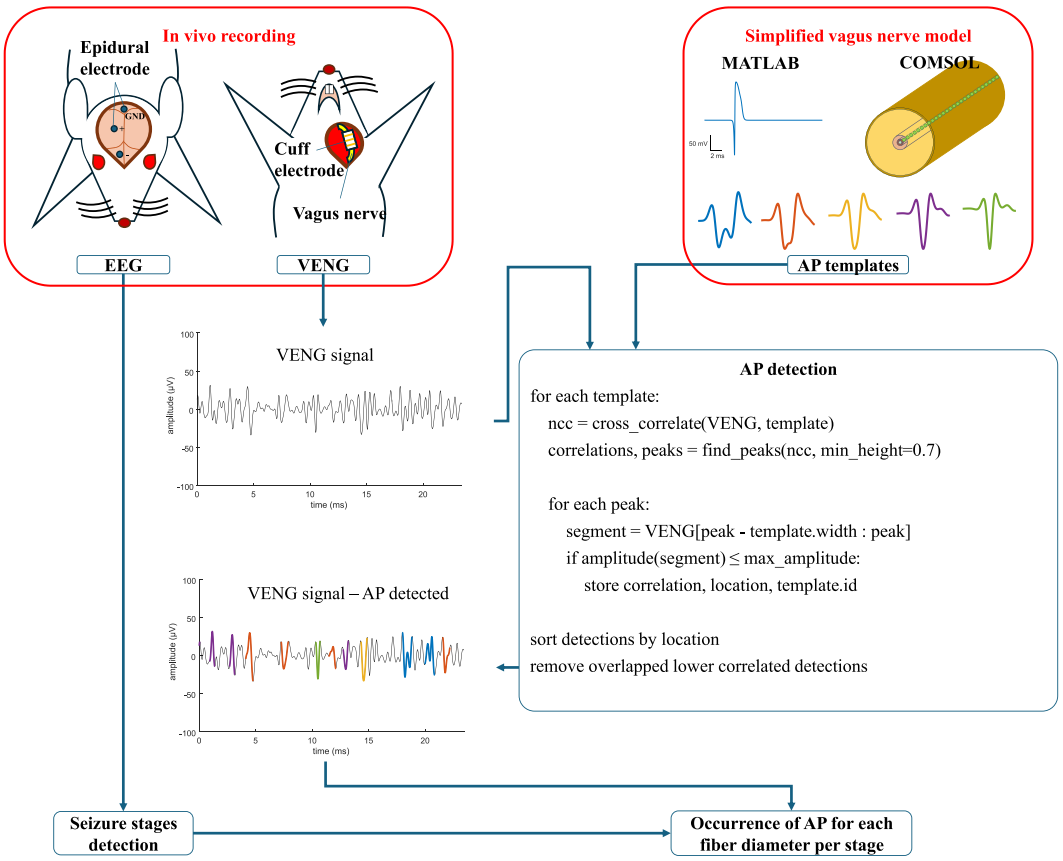

Figure 4. Overall methodology of the experiment. The vagus nerve electroneurogram (VENG) is processed offline using a template-matching algorithm (templates derived from a simplified vagus nerve model) to detect action potential (AP). The electroencephalogram (EEG) is used to detect the different seizure stages, and then, to calculate the occurrence detection for each template at every stage.

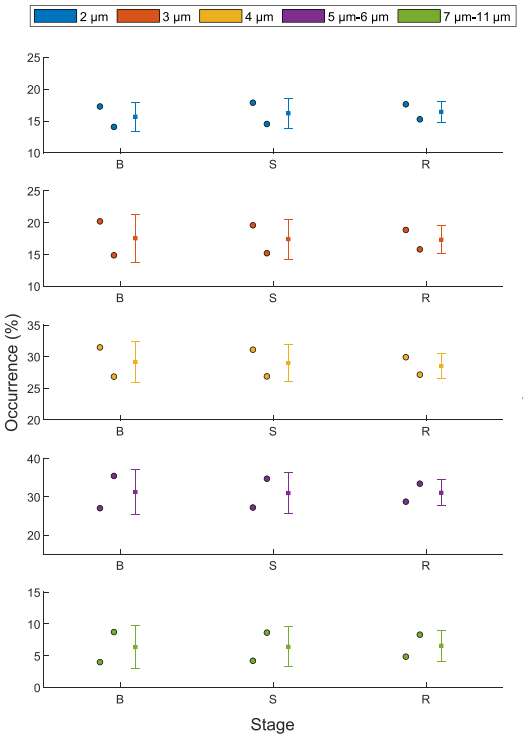

Figure 5. Occurrence of templates detection in the control group (n = 2) for each stage: baseline (B), saline (S) and recovery (R). The dots represent individual values, and the error bars represent the mean (squares) ± SD (whiskers) for each stage. There was no significant difference comparing to baseline percentage of occurrences.

Table 3. P-values obtained from multiple comparisons of the percentage of occurrence with respect to the baseline stage in the control group. No significant p-values were found.

	2 μm	3 μm	4 μm	5–6 μm	7–11 μm
vs Saline	0.64	1.00	1.00	1.00	1.00
Vs Recovery	0.64	1.00	1.00	1.00	1.00

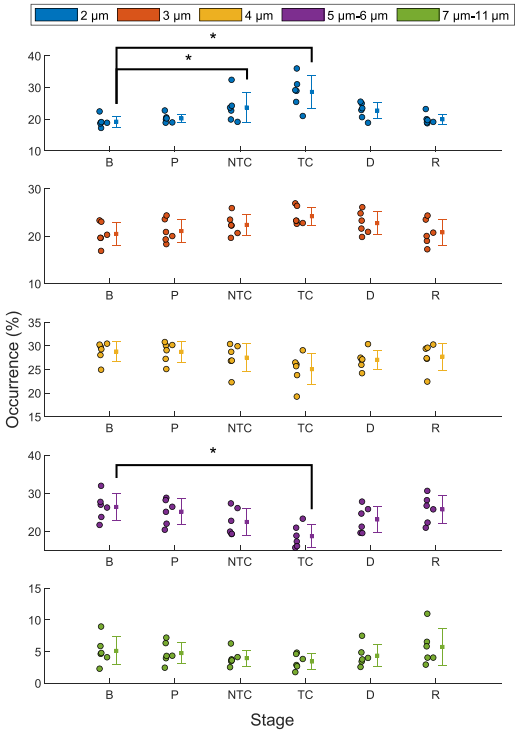

Figure 6. Occurrence of template detection for the PTZ group (n = 6) at every stage: baseline (B), pre-ictal (P), non-tonic–clonic-ictal (NTC), tonic–clonic (TC), EEG depression (D) and recovery (R). The dots represent individual values, and the error bars represent the mean (squares) ± SD (whiskers) for each stage. (*p-value < 0.05).

There is an increase in the percentage of APs associated with smaller diameter fibers (2 μm and 3 μm) during the seizure. The percentage of occurrence for the 2 μm fiber showed a significant change across the stages (p-value = 0.0017 < 0.05), while no significant change was observed for the 3 μm fiber (p-value = 0.19 > 0.05). In contrast, during the seizure progression, the percentage of occurrence decreased for larger diameter fibers (4 μm, 5–6 μm, and 7–11 μm). Among these, only the 5–6 μm fiber showed a significant change across the stages (p-value = 0.0184), whereas no significant changes were found for the 4 μm fiber (p-value = 0.16 > 0.05) r the 7–11 μm fibers (p-value = 0.43 > 0.05). For the post-hoc comparison with baseline, the 2 μm fiber exhibited significant changes during the Non-Tonic–Clonic Ictal and Tonic–Clonic stages (p-value = 0.0454 < 0.05 and p-value = 0.000 603 < 0.05, respectively). The 5–6 μm fiber significantly changed during the tonic–clonic stage (p-value = 0.009 73 < 0.05) (see table 4 for details).

For the absolute occurrence, there is a significant decrease in firing rate at the tonic–clonic stage for 3 μm, 4 μm, 5–6 μm, and 7–11 μm fibers. In contrast, no significant changes were observed for the 2 μm fibers (see figure S-2 in supplementary materials). This means that the increase in contribution to the percentage of occurrence in smaller diameter fibers (i.e. 2 μm and 3 μm) is mainly due to a reduction in contribution of large diameter fibers (i.e. 4 μm, 5–6 μm, and 7–11 μm fibers), hence decreasing the total number of firing fibers (i.e. all diameters).

The percentages of occurrence of the AP detected in the baseline of the control and the PTZ groups were compared. No significant differences were found between the fibers (2 μm, p-value = 0.14 > 0.05; 3 μm, p-value = 0.43 > 0.05; 4 μm, p-value = 0.86 > 0.05; 5–6 μm, p-value = 0.29 > 0.05; 7–11 μm, p-value = 1.0 > 0.05).

3.3. Correlation analysis

To rule out the possibility that neuronal discharge frequency influenced detection accuracy, the correlation values of detected APs were analyzed. For each rat, the median correlation was calculated at every stage to assess whether the templates continued to accurately

Table 4. P-values obtained from multiple comparisons of the percentage of occurrence with respect to the baseline stage. The significant p-values (<0.05) are highlighted in bold.

	2 μm	3 μm	4 μm	5–6 μm	7–11 μm
vs Pre-ictal	0.67	0.98	1.00	1.00	1.00
vs Non-Tonic–Clonic Ictal	**0.045**	0.67	0.84	0.30	0.59
vs Tonic–Clonic	**0.0006**	0.080	0.070	**0.0097**	0.38
vs EEG depression	0.061	0.38	0.55	0.51	0.87
vs Recovery	0.85	1.00	0.96	1.00	1.00

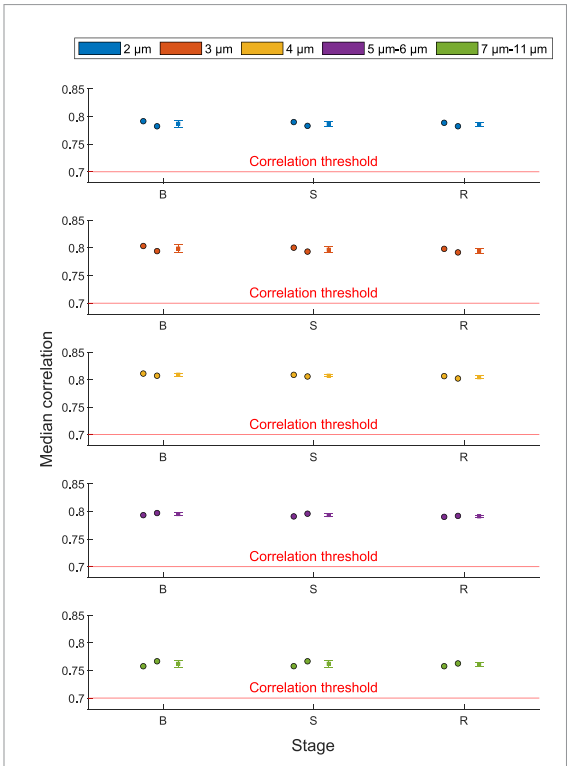

Figure 7. Median correlation of AP detected by each template in the control group (n = 2) at each stage: baseline (B), saline (S) and recovery (R). The dots represent individual values, and the error bars represent the mean (squares) ± SD (whiskers) for each stage .

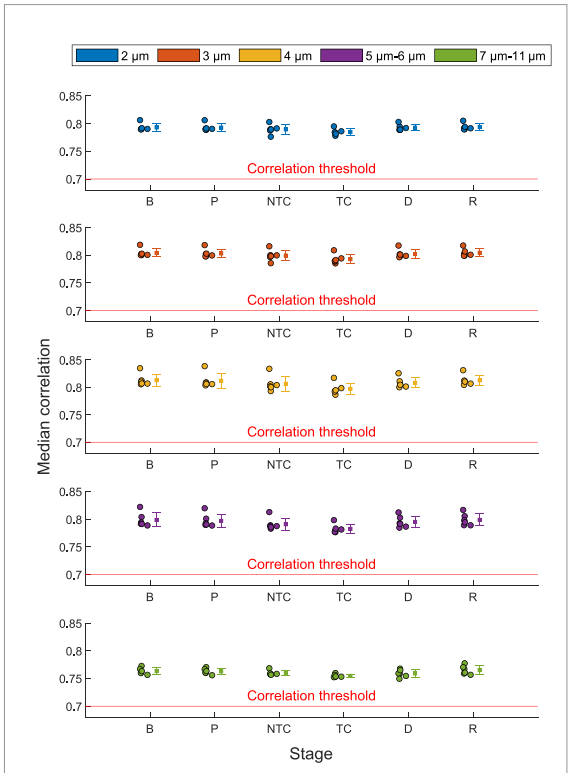

Figure 8. Median correlation of AP detected by each template in the control group (n = 6) at each stage: baseline (B), pre-ictal (P), non-tonic–clonic-ictal (NTC), tonic–clonic (TC), EEG depression (D) and recovery (R). The dots represent individual values, and the error bars represent the mean (squares) ± SD (whiskers) for each stage.

match the VENG signal. Figures 7 and 8 summarize the results for the control and PTZ groups, respectively.

In both the control group and the PTZ group, the median correlation for all templates remained stable. This indicates that the templates consistently fit the signal well across stages, supporting the interpretation that the reduction in detected spikes reflects an actual decrease in AP activity rather than a decline in detection accuracy.

4. Discussion

This work provides evidence that seizures modulate the fibers' activation in the vagus nerve. For the PTZ groups, the findings reveal a significant increase in the percentage of small-diameter active fibers (2 μm and 3 μm), corresponding to the expected increase in autonomic manifestations. We also observe a concurrent relative decrease in larger-diameter fiber activation (4 μm, 5–6 μm and 7–11 μm). None of those changes are found in the control group. This low percentage of occurrence in larger-diameter fiber activation could be explained by the fact that these fibers are predominantly associated with motor function [39], which is suppressed under anesthesia. During seizures, their activity may increase, but this effect could be masked by the predominant activation of smaller autonomic fibers, resulting in a lower relative contribution of larger fibers. This hypothesis warrants further investigation.

Regarding the current landscape of epilepsy treatments, particularly devices for VNS, this finding is appealing to target a novel biological marker allowing for closed-loop paradigms. The contrast between the resting state and epileptic seizures could be effectively used to detect seizures. This finding is particularly

promising given the anatomical similarities in vagus nerve fiber distribution across species, suggesting the potential translatability of these results from rodents to humans and other animals. Stakenborg *et al* reported that the cervical vagus nerve in humans, mice, and pigs contains similar percentages of myelinated fibers ($54 \pm 4\%$ in mice and $54 \pm 7\%$ in humans) [55]. Pelot *et al* reported a lower proportion of myelinated fibers ($\sim$20%) across mammalian species, while still emphasizing comparable numbers across species [56]. The general pattern of fiber-type composition and diameter–frequency distribution in the cervical vagus nerve is similar among mammals. Findings in larger animals, such as cats [57], rabbits [58], and ferrets [59], suggest that the same spectrum is broadly applicable across many species. However, caution is warranted before transferring conclusions to humans. Significant anatomical differences, such as the multifascicular structure in humans versus the often monofascicular structure in rats, must be considered when interpreting recordings [60].

This work has limitations that should be considered when interpreting the results. First, the VENG analysis does not include the unmyelinated C fibers, whose small diameters—hence small signal amplitude—do not allow for a nerve surface recording as implemented here [61]. This can limit physiological interpretation, considering that C-fibers are known to be primary contributors to autonomic regulation. However, this underrepresentation of small fibers does not impact the comparative analysis across different stages, as it does not alter the significant differences among stages. Second, we simulated a single, centrally placed fiber to simplify computation. Prior work [42] showed that while fiber position significantly affects the amplitude of the recorded AP (up to 60%), its shape—our primary focus—remains largely unchanged. Since our analysis is based on shape correlation, which is amplitude-invariant, this simplification seems justified. Nonetheless, we acknowledge that a more detailed model with multiple fibers could further enhance accuracy. Additionally, the current model of recording electrodes as point sources can be improved by modeling spatially extended metal contacts (see supplementary figures S-4 and S-5). Indeed, these metal contacts influence locally the voltage distribution and hence the recorded AP. Despite the high template similarity (correlation > 0.92), some differences in spike detection values were observed across configurations. However, the overall trends remained highly similar (see supplementary figure S-6–S-9), indicating that the same underlying physiological dynamics were captured. These findings suggest that general conclusions are not sensitive to the limited level of detail in the model. Nevertheless, our current approach represents a simpler first step and a valuable approximation for initial analyses of electrode-neuron interactions. We believe that this simplified model is adequate for a first study. The model focuses on accurately reproducing conduction velocity to obtain AP templates with faithful waveforms. Other parameters, such as waveform amplitude, may not be modeled with the same precision, but they are not used by the detection procedure and thus have less impact on the results. Third, the estimated diameters associated with each fiber type in rats may have overlapping ranges, making it challenging to attribute precise functions to individual fiber types based solely on diameter. Nevertheless, detecting a difference in vagus nerve activity remains a significant observation. Fourth, the study's small sample size, with only two healthy control rats and six epileptic rats (also used as their own control), limits the statistical power and generalizability. In that regard, statistically speaking, we mainly rely on using the six epileptic rats as their own controls, which is also appealing as it limits variability and makes it easier to compare ictal changes. Although the findings are statistically significant and suggest a consistent biological interpretation, future research with larger sample sizes is needed to confirm these results. By estimating the power of this study [62], the minimum sample size required to detect changes with a power greater than 80% is $n = 6$, which aligns with the significant changes observed in this study (in 2 μm and 5–6 μm fiber diameters). To detect significant changes across all fiber diameters (i.e., also 3 μm, 4 μm, and 7–11 μm), the minimum sample size is expected to be $n = 28$. The significant changes detected in 2 out of 5 templates are already sufficient for detecting seizures, and potential changes in other fiber types would likely be minor (given the results of this study). Still, further studies could increase the number of rats to increase the statistical power.

Future studies could incorporate improvements in the nerve model, adding an electrical representation of the myelin, using a double-cable model [63] and multiple fibers in the model. Also, a more accurate representation of the nerve's geometric and morphological features should be considered, including fascicle count, fascicle sizes, and perineurium thickness [60, 64], since these parameters have important effects on models of neural activity. Additionally, directionality of the AP can be an additional feature by classifying afferent and efferent activity. Furthermore, exploring various electrode dimensions and inter-electrode distances is essential, as these factors can directly influence the discrimination of fiber conduction velocities. Simultaneously, a sensitivity analysis should be conducted to evaluate how variations in input parameters, such as conductivity, affect the model's performance, as these parameters can vary across different sources and literature [46, 65]. Additionally, the confound EMG artifact must be addressed by incorporating simultaneous EMG monitoring electrodes to quantify artifact contributions. Future experimental designs should also consider performing nerve recordings

under paralysis with artificial ventilation to ensure no movement or EMG artifact [66, 67]. Finally, the predictive performance of this methodology for early seizure detection should be compared with established physiological markers like EMG [68, 69]. However, EMG is primarily effective for seizures with motor manifestations and is less suitable for non-motor seizure types, such as absence seizures [70]. In contrast, the proposed approach, which utilizes the same electrode for both stimulation and seizure detection, offers a practical advantage by streamlining the detection process. This methodology could be also translated to a chronic environment in healthy rats [71], and in epileptic models, such as kainic acid [72, 73], adapting the setup for long-term recording of the vagus nerve [74, 75].

This opens the door for the development of a novel approach to epilepsy management by analyzing vagus nerve activity with fiber-specific resolution. By distinguishing autonomic fiber activation during seizures, our approach offers insights into the autonomic dysregulation that often accompanies epileptic events. This could enable seizure detection and open avenues for targeted interventions, such as optimizing VNS protocols, providing personalized epilepsy treatments, and enhancing patient outcomes.

5. Conclusion

This work compared the activity of vagus nerve recordings before, during, and after seizures in epileptic rats. A significant increase was found in the percentage of small-diameter active fibers (2 μm and 3 μm), in line with increased autonomic manifestations expected during seizures. A concurrent relative decrease in larger-diameter fiber activation (4 μm, 5–6 μm, and 7–11 μm) was also noted. Our findings suggest that the percentage of occurrence of the active fibers could be used as a biomarker for seizure detection, providing insights for the development of a closed-loop VNS therapy.

Data availability statement

The data cannot be made publicly available upon publication because they are owned by a third party, and the terms of use prevent public distribution. The data that support the findings of this study are available upon reasonable request from the authors.

Acknowledgments

Q7
Q8

The research was financially supported by the Région Wallonne (Agreement N°8191, Belgium). We are grateful for the help provided by Geoffrey Vanbienne in the realization of our hardware setup and Michel Osée for the technical help provided.

Conflict of interest

Pascal Doguet and Jean Delbeke are shareholders of Synergia Medical.

Appendix A

The AP propagation model used the Hodgkin-Huxley equations coupled with the cable theory equations. Each term in the equation corresponds to a different contribution to the membrane potential:

- The capacitive current across the membrane is given by:

$$I_{C,x} = C_m \frac{d(V_{i,x} - V_{e,x})}{dt} \tag{A.1}$$

where $I_{C,x}$ is the membrane capacitive current density, C_m is the membrane capacitance per unit area, and $V_{i,x} - V_{e,x}$ is the transmembrane voltage at the node of Ranvier x.

- The ionic currents through the membrane channels are given by:

$$I_{ion,x} = i_{Na} + i_K + i_L \tag{A.2}$$

where $I_{ion,x}$ represents the ionic channels' current density per unit area at the node of Ranvier x, including sodium (i_{Na}), potassium (i_K), and leak (i_L) currents, which contribute to the overall flow of ions outward from the inside of the fiber.

The axial current flow between adjacent nodes of Ranvier is given by:

$$I_{NR,x} = \frac{V_{i,x-1} - 2V_{i,x} + V_{i,x+1}}{R_i} \tag{A.3}$$

where $I_{NR,x}$ represents the current propagation at the Node of Ranvier x (the adjacent nodes: $x-1$ and $x+1$), $V_{i,x}$ is the intracellular potential at the Node, and R_i is the internodal resistance.

- The internodal resistance is given by:

$$R_i = \rho_a \frac{L_{internode}}{\frac{\pi}{4} d_{axon}^2} \tag{A.4}$$

where $L_{internode}$, d_{axon}, and ρ_a represent the internodal distance, the diameter of the axon, and the axoplasmic resistivity, respectively.

Based on Kirchhoff's Current Law, the sum of the currents flowing out of the node (capacitive current $I_{C,x}$ and ionic currents $I_{ion,x}$) must equal the sum of the currents flowing into the node (axial current $I_{NR,x}$). It is important to note that both $I_{C,x}$ and $I_{ion,x}$ are current densities (in $\frac{A}{m^2}$); therefore, they must be multiplied by the surface area of the membrane at the

Table 5. Physiological parameters of the Wesselink model. Adapted from, with permission from Springer Nature. Adapted from [45], with permission from Springer Nature.

Parameter	Symbol	Value [unit]
Membrane capacity	c_{m}	0.028 $\left[\frac{\mathrm{F}}{\mathrm{m}^2}\right]$
Leakage conductance	g_{L}	600 $\left[\frac{\mathrm{S}}{\mathrm{m}^2}\right]$
Sodium permeability	p_{Na}	0.0704
Potassium conductance	g_{K}	300 $\left[\frac{\mathrm{S}}{\mathrm{m}^2}\right]$
Intra-axonal resistance	ρ_{a}	0.33 $[\Omega m]$
Leakage equilibrium potential	V_{L}	-84.14 [mV]
Sodium equilibrium potential	V_{Na}	43.7 [mV]
Sodium concentration outside the cell	$\mathrm{Na_o}$	154 [mM]
Sodium concentration inside the cell	Na_{i}	30 [mM]
Potassium equilibrium potential	V_{K}	-84 [mV]
Resting membrane potential	V_{r}	-84 [mV]
Faraday constant	F	96, 485 $\left[\frac{\mathrm{C}}{\mathrm{mole}}\right]$
Gas constant	R	8.3144 $\left[\frac{\mathrm{J}}{\mathrm{Kmol}}\right]$

node to compute the related currents. Assuming a cylindrical geometry at the node, the surface area is represented by:

$$A_x = \pi\, d_{\mathrm{axon}} l_x \tag{A.5}$$

where represents the length of the node x and d_{axon} is the diameter of the axon. This results in the equation governing the electrical behavior at a node of Ranvier x, given by:

$$I_{\mathrm{NR},x} = A_x \left(I_{\mathrm{C},x} + I_{\mathrm{ion},x}\right) \quad . \tag{A.6}$$

Wesselink–Schwarz [44, 45] adapted this model to better reflect the biophysical properties of mammalian axons by modifying the equations that govern ion channel dynamics. This adaptation includes parameters of the fiber model (see table 5) and specific equations for sodium, potassium, and leakage currents:

- The sodium current is given by:

$$i_{\mathrm{Na}} = \frac{m^3 \cdot h \cdot p_{\mathrm{Na}} \cdot V \cdot F^2}{R \cdot T} \times \frac{\left(\mathrm{Na_o} - \mathrm{Na_i} \cdot \mathrm{e}^{\frac{V \cdot F}{R \cdot T}}\right)}{1 - \mathrm{e}^{\frac{V \cdot F}{R \cdot T}}} \tag{A.7}$$

  where i_{Na} is the sodium current density, is the membrane voltage, p_{Na} is sodium permeability, Na_o and $\mathrm{Na_i}$ represent the sodium concentration outside and inside the cell respectively, R is the gas constant, F is the Faraday constant, T is the absolute temperature, and m and h represent the probability that the sodium channel is open at a given moment in time, i.e., the proportion of sodium channels in which, respectively the activation or inactivation gate, is open.
- The potassium current is given by:

$$i_{\mathrm{K}} = n^4 \cdot g_{\mathrm{K}} \cdot (V - V_{\mathrm{K}}) \tag{A.8}$$

  where is the potassium current density, V_{k} is the potassium equilibrium potential, and g_{k} is potassium conductance, and n represents the probability that the potassium channel is open at a given moment, i.e., the proportion of potation channels in which the activation gate is open.
- The leakage current is given by:

$$i_{\mathrm{L}} = g_{\mathrm{L}} \cdot (V - V_{\mathrm{L}}) \tag{A.9}$$

  where i_{L} is the leakage current density, V_{L} is the leakage equilibrium potential, and g_{L} is the leakage conductance.

The terms m, h and n represent the probability of ion channels being in an open or closed state. These variables follow first-order differential equations, given by:

$$\frac{\mathrm{d}m}{\mathrm{d}t} = a_m \cdot (1 - m) - b_m \cdot m, m(0) = 0.0382 \tag{A.10}$$

$$\frac{\mathrm{d}h}{\mathrm{d}t} = a_h \cdot (1 - h) - b_h \cdot h, h(0) = 0.6986 \tag{A.11}$$

$$\frac{\mathrm{d}n}{\mathrm{d}t} = a_n \cdot (1 - n) - b_n \cdot n, n(0) = 0.2563. \tag{A.12}$$

The functions a and b determine the transition rates between the open and closed states of these channels, given by:

$$a_m = \frac{Q_{10} \cdot 4.6 \cdot 10^3 \,(V + 18.4)}{\left(1 - \mathrm{e}^{\left(\frac{-18.4 - V}{10.3}\right)}\right)} \tag{A13}$$

$$b_m = \frac{Q_{10} \cdot 0.33 \cdot 10^3 \cdot (-22.7 - V)}{\left(1 - \mathrm{e}^{\left(\frac{V + 22.7}{9.16}\right)}\right)} \tag{A.14}$$

$$a_h = \frac{Q_{10} \cdot 0.21 \cdot 10^3 \cdot (-111 - V)}{\left(1 - \mathrm{e}^{\left(\frac{V + 111}{11}\right)}\right)} \tag{A.15}$$

$$b_h = \frac{Q_{10} \cdot 14.1 \cdot 10^3}{\left(1 - e^{\left(\frac{-28.8-V}{13.4}\right)}\right)} \tag{A.16}$$

$$a_n = \frac{Q_{10} 51.7\,(V + 93.2)}{\left(1 - e^{\left(\frac{-93.2-V}{1.1}\right)}\right)} \tag{A.17}$$

$$b_n = \frac{Q_{10} \cdot 92 \cdot (-76 - V)}{\left(1 - e^{\left(\frac{V+76}{10.5}\right)}\right)} \tag{A.18}$$

where $Q_{10} = 3^{(31.9-37)/10} = 0.571$, relative to the reference temperature of 37 °C.

Appendix B

The 3D FEM of the vagus nerve was governed by the following equations of current conservation (all domains):

$$\nabla \cdot J = Q_{j,v} \tag{B.1}$$

$$J = \sigma E + \frac{\delta D}{\delta t} + J_e \tag{B.2}$$

$$E = -\nabla V \tag{B.3}$$

$$D = \epsilon_0 \epsilon_r E \tag{B.4}$$

where j is the total electric current density, J_e is the external current density (neglected), E is the scalar electric field, D is the electric displacement field, V is the voltage, σ is the electrical conductivity (defined for each material, see table 1), E_0 is the permittivity of free space (8.85×10^{-12} F m^{-1}) and E^T is the relative permittivity (=1).

The boundary condition on the medium's surface was defined as a distributed surface impedance:

$$\hat{n} \cdot J_m = \frac{1}{d_s}\left(\sigma + \epsilon_0 \epsilon_r \frac{\delta}{\delta t}\right)(V - V_{ref}) \tag{B.5}$$

where j_m is the current density through the surface, n is a unit vector perpendicular to the surσface, d_s is the thickness of the surface layer (=0.05 m). The electrical conductivity () was set as 0.02 S m^{-1}. V_{ref} is the voltage reference (=0 V) where the medium's surface is tied to ground.

Finally, each node of Ranvier was set as a current source (current density), which contributed to the current conservation of the domains (q_{jv})

Table 6. Single point electrode positions along the nerve model and simulation times.

Fiber size model (μm)	Single points position (mm)	Simulation time (ms)
2	10 ; 14	4
3	15 ; 19	4
4	20 ; 24	3.5
5	25 ; 29	3.5
6	30 ; 34	3.5
7	35 ; 39	3.5
8	40 ; 44	3.5
9	45 ; 49	3
10	50 ; 54	3
11	55 ; 59	3

Appendix C

Each model has a vagus nerve length of 0.206 m and has 150 nodes of Ranvier. Since the number of nodes of Ranvier was fixed across all fibers, but the internodal distance varied proportionally with fiber diameter (internodal length = 100 × diameter), the spatial distribution of nodes differed for each fiber size. To capture action potential propagation centered in time using COMSOL, the pair of single-point electrodes was therefore positioned at different locations along the models. The simulation times and single points electrode positions used are shown in table 6. The radial position of the single points electrodes is 310.5 μm, having a gap of 70.5 μm.

ORCID iDs

Javier Chávez Cerda 0000-0003-1155-6701
Louis Vande Perre 0000-0003-3401-2993
Romain Raffoul 0000-0002-1439-0367
Maxime Verstraeten 0000-0001-8882-6541
Enrique Germany Morrison 0000-0002-3100-187X
Hugo Smets 0000-0002-5649-6389
Pascal Doguet 0009-0003-3139-0080
Jean Delbeke 0000-0001-9542-3599
Riëm El Tahry 0000-0002-2440-0194
Antoine Nonclercq 0000-0003-0292-9588

References

[1] Brodie M J, Barry S J E, Bamagous G A, Norrie J D and Kwan P 2012 Patterns of treatment response in newly diagnosed epilepsy *Neurology* **78** 1548–54
[2] Beghi E 2020 The epidemiology of epilepsy *Neuroepidemiology* **54** 185–91
[3] Alarcón G and Valentín A 2012 *Introduction to Epilepsy* (Cambridge University Press)
[4] Baker G A, Jacoby A, Buck D, Stalgis C and Monnet D 1997 Quality of life of people with epilepsy: a European study *Epilepsia* **38** 353–62
[5] Raedt R, Durand D M, Boon P, Vonck K and Krames E S 2018 *Chapter 81—Epilepsy: Anatomy, Physiology, Pathophysiology, and Disorders* (Second Edi. Elsevier Ltd) (https://doi.org/10.1016/B978-0-12-805353-9.00081-4)

[6] Kwan P and Brodie M J 2000 Early identification of refractory epilepsy *N. Engl. J. Med.* **342** 314–9
[7] Mohanraj R and Brodie M J 2006 Diagnosing refractory epilepsy: response to sequential treatment schedules *Eur. J. Neurol.* **13** 277–82
[8] Hitiris N, Mohanraj R, Norrie J, Sills G J and Brodie M J 2007 Predictors of pharmacoresistant epilepsy *Epilepsy Res.* **75** 192–6
[9] Kwan P and Brodie M J 2001 Effectiveness of first antiepileptic drug *Epilepsia* **42** 1255–60
[10] Patsalos P N and Duncan J S 1993 Antiepileptic drugs: a review of clinically significant drug interactions *Drug Saf.* **9** 156–84
[11] Camfield P and Camfield C 1994 Acute and chronic toxicity of antiepileptic medications: a selective review *J. Can. Des Sci. Neurol.* **21** S7–S11
[12] Engel J 2013 *Seizures and Epilepsy* vol 83 (Oxford University Press)
[13] Englot D J, Rolston J D, Wright C W, Hassnain K H and Chang E F 2016 Rates and predictors of seizure freedom with vagus nerve stimulation for intractable epilepsy *Neurosurgery* **79** 345–53
[14] Englot D J, Raygor K P, Molinaro A M, Garcia P A, Knowlton R C, Auguste K I and Chang E F 2014 Factors associated with failed focal neocortical epilepsy surgery *Neurosurgery* **75** 648–55
[15] Englot D J, Han S J, Rolston J D, Ivan M E, Kuperman R A, Chang E F, Gupta N, Sullivan J E and Auguste K I 2014 Epilepsy surgery failure in children: a quantitative and qualitative analysis *J. Neurosurg. Pediatr.* **14** 386–95
[16] Ryvlin P, Rheims S, Hirsch L J, Sokolov A and Jehi L 2021 Neuromodulation in epilepsy: state-of-the-art approved therapies *Lancet Neurol.* **20** 1038–47
[17] Afra P, Adamolekun B, Aydemir S and Watson G D R 2021 Evolution of the vagus nerve stimulation (VNS) therapy system technology for drug-resistant epilepsy *Front. Med. Technol.* **3** 696543
[18] Marrosu F, Serra A, Maleci A, Puligheddu M, Biggio G and Piga M 2003 Correlation between GABAA receptor density and vagus nerve stimulation in individuals with drug-resistant partial epilepsy *Epilepsy Res.* **55** 59–70
[19] Berger A, Vespa S, Dricot L, Dumoulin M, Vandewalle G and Tahry R E 2021 How is the norepinephrine system involved in the antiepileptic effects of vagus nerve stimulation? *Front. Neurosci.* **15** 790943
[20] Krahl S E and Clark K B 2012 Vagus nerve stimulation for epilepsy: a review of central mechanisms *Surg. Neurol. Int.* **3** S255
[21] Wheless J W, Gienapp A J and Ryvlin P 2018 Vagus nerve stimulation (VNS) therapy update *Epilepsy Behav.* **88** 2–10
[22] De Faria G M, Tobaldini E, Montano N, Cunha T S, Casali K R and De Amorim H A 2024 Advances in non-invasive neuromodulation : designing closed-loop devices for respiratory-controlled transcutaneous vagus nerve stimulation *Healthcare* **12** 22
[23] Morris GL III and Mueller W M 1999 Long-term treatment with vagus nerve stimulation in patients with refractory epilepsy *Neurology* **53** 1731
[24] Ben-Menachem E 2001 Vagus nerve stimulation, side effects, and long-term safety *J. Clin. Neurophysiol.* **18** 415–8
[25] Aalbers M, Vles J, Klinkenberg S, Hoogland G, Majoie M and Rijkers K 2011 Animal models for vagus nerve stimulation in epilepsy *Exp. Neurol.* **230** 167–75
[26] Winston G M, Guadix S, Lavieri M T, Uribe-Cardenas R, Kocharian G, Williams N, Sholle E, Grinspan Z and Hoffman C E 2021 Closed-loop vagal nerve stimulation for intractable epilepsy: a single-center experience *Seizure* **88** 95–101
[27] Eggleston K S, Olin B D and Fisher R S 2014 Ictal tachycardia: the head-heart connection *Seizure* **23** 496–505
[28] Fisher R S *et al* 2016 Automatic vagus nerve stimulation triggered by ictal tachycardia: clinical outcomes and device performance—The U.S. E-37 trial *Neuromodulation* **19** 188–95
[29] Hampel K G, Vatter H, Elger C E and Surges R 2015 Cardiac-based vagus nerve stimulation reduced seizure duration in a patient with refractory epilepsy *Seizure* **26** 81–85
[30] Stumpp L, Smets H, Vespa S, Cury J, Doguet P, Delbeke J, Nonclercq A and El Tahry R 2021 Vagus nerve electroneurogram-based detection of acute pentylenetetrazol induced seizures in rats *Int. J. Neural Syst.* **31** 2150024
[31] Chávez Cerda J *et al* 2024 Proof-of-concept of respiration-triggered vagus nerve stimulation to treat epilepsy *2024 IEEE Int. Symp. on Medical Measurements and Applications (Memea)* pp 1–6
[32] Chávez Cerda J *et al* 2022 Micro cuff electrode manufacture for vagus nerve monitoring in rats *2022 IEEE Biomedical Circuits and Systems Conf. (Biocas) (Taipei, Taiwan)* pp 434–8
[33] Harreby K R, Sevcencu C and Struijk J J 2011 Ictal and perictal changes in cervical vagus nerve activity associated with cardiac effects *Med. Biol. Eng. Comput.* **49** 1025–33
[34] Stumpp L *et al* 2020 Recording of spontaneous vagus nerve activity during pentylenetetrazol-induced seizures in rats *J. Neurosci. Methods* **343** 108832
[35] Acedo Reina E, Germany Morrison E, Dereli A S, Collard E, Raffoul R, Nonclercq A and El Tahry R 2024 Vagus nerve electroneurogram-based detection of acute kainic acid induced seizures *Front. Neurosci.* **18** 1–12
[36] Brotherstone R and McLellan A 2012 Parasympathetic alteration during sub-clinical seizures *Seizure* **21** 391–8
[37] Jeppesen J, Fuglsang-Frederiksen A, Brugada R, Pedersen B, Rubboli G, Johansen P and Beniczky S 2014 Heart rate variability analysis indicates preictal parasympathetic overdrive preceding seizure-induced cardiac dysrhythmias leading to sudden unexpected death in a patient with epilepsy *Epilepsia* **55** 67–71
[38] Ahmed U, Chang Y C, Zafeiropoulos S, Nassrallah Z, Miller L and Zanos S 2022 Strategies for precision vagus neuromodulation *Bioelectron. Med.* **8** 9
[39] Yap J Y Y, Keatch C, Lambert E, Woods W, Stoddart P R and Kameneva T 2020 Critical review of transcutaneous vagus nerve stimulation: challenges for translation to clinical practice *Front. Neurosci.* **14** 284
[40] Schnitzlein H N, Rowe L C and Hoffman H H 1958 The myelinated component of the vagus nerves in man *Anat. Rec.* **131** 649–67
[41] Raffoul R *et al* 2022 Action potential detection algorithm adaptable to individual nerve and recording setup *2022 IEEE Biomedical Circuits and Systems Conf. (Biocas) (Taipei, Taiwan)* pp 655–9
[42] Smets H *et al* 2021 Analysing vagus nerve spontaneous activity using finite element modelling *J. Neural Eng.* **18** 56008
[43] Chávez Cerda J *et al* 2025 The effect of vagus nerve stimulation on heart rate and respiration rate and their impact on seizure susceptibility in anaesthetized rats under pentylenetetrazol *Front. Neurosci.* **19** 1487082
[44] Schwarz J R, Reid G and Bostock H 1995 Action potentials and membrane currents in the human node of Ranvier *Pflugers Arch.* **430** 283–92
[45] Wesselink W A, Holsheimer J and Boom H B K 1999 A model of the electrical behaviour of myelinated sensory nerve fibres based on human data *Med. Biol. Eng. Comput.* **37** 228–35
[46] Arle J E, Carlson K W and Mei L 2016 Investigation of mechanisms of vagus nerve stimulation for seizure using finite element modeling *Epilepsy Res.* **126** 109–18
[47] Licursi de Alcântara A C, Salgado H C and Sassoli Fazan V P 2008 Morphology and morphometry of the vagus nerve in male and female spontaneously hypertensive rats *Brain Res.* **1197** 170–80
[48] McNeal D R 1976 Analysis of a model for excitation of myelinated nerve *IEEE Trans. Biomed. Eng.* **BME-23** 329–37

[49] Chomiak T and Hu B 2009 What is the optimal value of the g-ratio for myelinated fibers in the rat CNS? A theoretical approach *PLoS One* **4** e7754

[50] Sweeney J D, Mortimer J T and Durand D 1987 Modeling of mammalian myelinated nerve for functional neuromuscular stimulation *IEEE 9th Annual Conf. of the Engineering in Medicine and Biology Society* pp 1577–8

[51] Woodbury J W and Woodbury D M 1991 Vagal stimulation reduces the severity of maximal electroshock seizures in intact rats: use of a cuff electrode for stimulating and recording *Pacing Clin. Electrophysiol.* **14** 94–107

[52] Furniturewalla A, Rustogi P, Patrick E and Judy J W 2019 Modeling the recording of intraneural action potentials with microelectrodes using fem and point-source methods *Int. IEEE/EMBS Conf. Neural Eng. NER* **2019** 1191–4

[53] McKight P E and Najab J 2010 Kruskal-wallis test *Orsini Encycl. Psycholl.* 1

Q11

[54] Dunnett C W 1955 A multiple comparison procedure for comparing several treatments with a control *J. Am. Stat. Assoc.* **50** 1096–121

[55] Stakenborg N, Gomez-Pinilla P J, Verlinden T J M, Wolthuis A M, D'Hoore A, Farré R, Herijgers P, Matteoli G and Boeckxstaens G E 2020 Comparison between the cervical and abdominal vagus nerves in mice, pigs, and humans *Neurogastroenterol. Motil.* **32** 1–8

[56] Pelot N A and Grill W M 2018 Effects of vagal neuromodulation on feeding behavior *Brain Res.* **1693** 180–7

[57] Agostoni E, Chinnock J E, Daly M D B and Murray J 1957 Functional and histological studies of the vagus nerve and its branches to the heart, lungs and abdominal viscera in the cat *J. Physiol.* **135** 182

[58] Evans D H L and Murray J 1954 Histological and functional studies on the fibre composition of the vagus nerve of the rabbit *J. Anat.* **88** 320

[59] Asala S A and Bower A J 1986 An electron microscope study of vagus nerve composition in the ferret *Anat. Embryol.* **175** 247–53

[60] Pelot N A, Goldhagen G B, Cariello J E, Musselman E D, Clissold K A, Ezzell J A and Grill W M 2020 Quantified morphology of the cervical and subdiaphragmatic vagus nerves of human, pig, and rat *Front. Neurosci.* **14** 1–19

[61] Schmelz M and Schmidt R 2010 Microneurographic single-unit recordings to assess receptive properties of afferent human C-fibers *Neurosci. Lett.* **470** 158–61

[62] Mahoney M and Magel R 1996 Estimation of the power of the Kruskal-Wallis test *Biom. J.* **38** 613–30

[63] McIntyre C C, Richardson A G and Grill W M 2002 Modeling the excitability of mammalian nerve fibers: influence of after potentials on the recovery cycle *J. Neurophysiol.* **87** 995–1006

[64] Musselman E D, Raha I, Pelot N A and Grill W M 2025 Scaling of vagus nerve stimulation parameters does not achieve equivalent nerve responses across species *Bioelectron. Med.* **11** 11

[65] Pelot N A, Behrend C E and Grill W M 2018 On the parameters used in finite element modeling of compound peripheral nerves *J. Neural Eng.* **16** 16007

[66] RoaFiore L, Meyer T, Peixoto T and Irazoqui P 2024 Label-free functional imaging of vagus nerve stimulation-evoked potentials at the cortical surface *npj Biosensing* **1** 1–11

[67] Horn C C and Friedman M I 2003 Detection of single unit activity from the rat vagus using cluster analysis of principal components *J. Neurosci. Methods* **122** 141–7

[68] Beniczky S, Wiebe S, Jeppesen J, Tatum W O, Brazdil M, Wang Y, Herman S T and Ryvlin P 2021 Automated seizure detection using wearable devices: a clinical practice guideline of the international league against epilepsy and the international federation of clinical neurophysiology *Clin. Neurophysiol.* **132** 1173–84

[69] Baumgartner C, Baumgartner J, Lang C, Lisy T and Koren J P 2025 Seizure detection devices *J. Clin. Med.* **14** 863

[70] Collard E, Germany Morrison E, Reina E A, Dereli A S, Apaire A, Nonclercq A and El Tahry R 2025 Vagal nerve signals are modulated by spontaneous seizures in genetic absence epilepsy rats from Strasbourg *Front. Neurosci.* **19** 1568261

[71] Smets H, Stumpp L, Chavez J, Cury J, Vande Perre L, Doguet P, Vanhoestenberghe A, Delbeke J, El Tahry R and Nonclercq A 2022 Chronic recording of the vagus nerve to analyze modulations by the light–dark cycle *J. Neural Eng.* **19** 046008

[72] Chávez Cerda J *et al* 2022 Chronic setup system for continuous monitoring of epileptic rats *2022 IEEE Biomedical Circuits and Systems Conf. (Biocas)* (*Taipei, Taiwan*) pp 591–4

[73] Bertoglio D, Amhaoul H, Van Eetveldt A, Houbrechts R, Van De Vijver S, Ali I and Dedeurwaerdere S 2017 Kainic acid-induced post-status epilepticus models of temporal lobe epilepsy with diverging seizure phenotype and neuropathology *Front. Neurol.* **8** 1–13

[74] Nonclercq A and Mathys P 2004 Reduction of power line interference using active electrodes and a driven-right-leg circuit in electroencephalographic recording with a minimum number of electrodes *Annual Int. Conf. of the IEEE Engineering in Medicine and Biology—Proc.*

[75] Nonclercq A and Mathys P 2010 Quantification of motion artifact rejection due to active electrodes and driven-right-leg circuit in spike detection algorithms *IEEE Trans. Biomed. Eng.* **57** 2746–52